

Multistage and passive cooling process driven by salinity difference

Original

Multistage and passive cooling process driven by salinity difference / Alberghini, Matteo; Morciano, Matteo; Fasano, Matteo; Bertiglia, Fabio; Fernicola, Vito; Asinari, Pietro; Chiavazzo, Eliodoro. - In: SCIENCE ADVANCES. - ISSN 2375-2548. - ELETTRONICO. - 6:11(2020), p. eaax5015. [10.1126/sciadv.aax5015]

Availability:

This version is available at: 11583/2803232 since: 2020-04-18T17:38:11Z

Publisher:

AAAS - American Association for the Advancement of Science

Published

DOI:10.1126/sciadv.aax5015

Terms of use:

This article is made available under terms and conditions as specified in the corresponding bibliographic description in the repository

Publisher copyright

(Article begins on next page)

Supplementary Materials for

Multistage and passive cooling process driven by salinity difference

Matteo Alberghini, Matteo Morciano, Matteo Fasano, Fabio Bertiglia, Vito Fericola, Pietro Asinari*, Eliodoro Chiavazzo*

*Corresponding author. Email: eliodoro.chiavazzo@polito.it (E.C.); pietro.asinari@polito.it (P.A.)

Published 13 March 2020, *Sci. Adv.* 6, eaax5015 (2020)

DOI: 10.1126/sciadv.aax5015

The PDF file includes:

- Note S1. Membrane permeability measurement
- Note S2. Measurement uncertainty analysis
- Note S3. Solute transport through the condensing side
- Note S4. Exergy analysis of the passive cooler
- Note S5. Comparison with other passive cooling approaches
- Note S6. Details on the coupling between passive distiller and cooler
- Note S7. Coefficient of performance
- Note S8. Coupling with high-salinity brines produced by different desalination technologies
- Note S9. Cost analysis of the laboratory-scale prototypes
- Note S10. Considerations on environmental and life-cycle analysis issues of the passive cooler
- Note S11. Cooling performance of the device under the sun
- Note S12. Durability and corrosion of the passive cooler
- Note S13. Boundary effects on the temperature field in the evaporator
- Fig. S1. Experimental setup to measure cooling capacity.
- Fig. S2. Assembly of the passive cooling device.
- Fig. S3. Natural mass transport phenomena in the present passive cooler.
- Fig. S4. Distillate consumption by the passive cooler.
- Fig. S5. Experimental results and modeling predictions of membrane permeability.
- Fig. S6. Possible spacer for enhancing the cooler performance.
- Fig. S7. Distillate consumption by the passive cooler for different air gaps.
- Fig. S8. Qualitative thermodynamic cycle of a passive solar cooling cycle.
- Fig. S9. Coupling between the passive cooler and distiller to implement a stable cooling cycle.
- Fig. S10. Mirror screening of the cooler exposed to the sun.
- Fig. S11. SIMSCAPE implementation of the mirror screening of the cooler exposed to the sun.
- Fig. S12. Lumped model for the heat transfer in the passive cooler.
- Fig. S13. Temperature profiles across the cooling stages in case of a 1-, 4-, and 10-stage configuration device.
- Fig. S14. Results of the finite element model for the hydrophilic layer (evaporator).

Fig. S15. Passive cooler operating with high-salinity brines produced by different desalination technologies.

Table S1. Uncertainties in the theoretical model.

Table S2. Exergy performance of the passive cooler with different number of stages.

Table S3. Estimated costs for the prototype of passive cooler.

Table S4. Estimated costs for the prototype of passive distiller considered here to implement a solar cooling cycle.

Table S5. Parameters considered for the simulations of the cooler performance under the sun.

References (41–75)

Other Supplementary Material for this manuscript includes the following:

(available at advances.sciencemag.org/cgi/content/full/6/11/eaax5015/DC1)

Dataset S1 (Microsoft Excel format). Experimental raw data of tests with NaCl.

Dataset S2 (Microsoft Excel format). Experimental raw data of tests with CaCl₂.

Note S1. Membrane permeability measurement

The hydrophobic microporous membrane employed in the passive cooling device is made of polytetrafluoroethylene, and it is characterised by pores with nominal diameter of 1.0 μm (*ANOW Microfiltration*). To validate the lumped parameter model in equation (13), the permeability (K) of the membrane is experimentally measured by means of a diffusion cell (*PermeGear 15 mm Side Bi Side Cell*, 7 mL volume).

Such experimental setup is composed by two cavities filled respectively with distilled and salt water separated from each other by the hydrophobic membrane, which is in direct contact with the two solutions. Each chamber communicates with the environment through a graduated capillary tube, which allows to visualize the free surface of liquid. If the two cavities are kept at the same temperature during experiments, water vapour flows through the membrane following the activity gradient, namely from distilled to salt water side, and this causes a variation in the liquid levels in both capillary tubes. The water level at the salt water side is measured every hour with a high-resolution camera, in order to evaluate the specific mass flow rate (J^*) of water vapour through the membrane. The average air temperature (T_A) of the room is monitored by an ambient thermometer. Two magnetic stirrers are used to avoid both ion polarization and temperature boundary layer at each side of the membrane. The membrane permeability can be then computed as

$$K = \frac{J^*}{A \Delta p_v} \quad (\text{S1})$$

where A is the active surface of the membrane and Δp_v is the vapour pressure difference across the membrane, which depends on the temperature and activity coefficients of water in the two solutions. Notice that J^* is computed by linearly fitting (least square method) the salt water level measured in the graduated capillary tube with time, over more than 9 hours of test.

Five independent measurements of membrane permeability have been carried out, and the following results obtained: $(6.4 \pm 1.0) \times 10^{-7} \text{ kg m}^{-2} \text{ Pa}^{-1} \text{ s}^{-1}$; $(5.9 \pm 0.9) \times 10^{-7} \text{ kg m}^{-2} \text{ Pa}^{-1} \text{ s}^{-1}$; $(8.7 \pm 1.2) \times 10^{-7} \text{ kg m}^{-2} \text{ Pa}^{-1} \text{ s}^{-1}$; $(6.7 \pm 1.0) \times 10^{-7} \text{ kg m}^{-2} \text{ Pa}^{-1} \text{ s}^{-1}$; $(6.2 \pm 1.0) \times 10^{-7} \text{ kg m}^{-2} \text{ Pa}^{-1} \text{ s}^{-1}$. Finally, results have been averaged and the expanded uncertainty estimated considering a coverage factor $k = 2$, which for a normally distributed probability is equivalent to a confidence interval of 95% (see **Supplementary Note 2** for details on the uncertainty estimation). The experimental result and modelling prediction of membrane permeability are compared in **Supplementary Fig. S5**.

Note that, during experiments, the Liquid Entry Pressure – LEP of the membranes is never exceeded. On the one side, the PTFE membrane considered for the distiller has pore size equal to $3.0 \mu\text{m}$, which corresponds to a LEP approximately equal to 0.25 bar (19). Since the passive distiller is fed by capillarity alone, the net pressure acting on the membrane is only due to the weight of the device. In the worst case, namely a 10-stage distiller, the bottom distillation stage is subject to approximately 3 mbar due to the weight of the nine stages above, that is eighty times lower than the LEP. In fact, we never observed water infiltration during our experiments (19). On the other side, the PTFE membrane considered for the cooler has pore size equal to $1.0 \mu\text{m}$, which corresponds to a LEP approximately equal to 0.8 bar. In this case, the salt water in the

condenser is pressurized by the small hydraulic head (≈ 15 cm) provided by the upper salt water basin. Again, the resulting pressure (15 mbar) is largely smaller with respect to the LEP.

Note S2. Measurement uncertainty analysis

The uncertainties of experimental measurements can be divided into two categories: uncertainty components estimated from the statistical analysis of the measured values (type A evaluation); uncertainty components estimated by other means, from *a priori* information such as calibration, resolution and accuracy of each measuring instrument employed (type B evaluation). Both contributions could be then used to estimate the combined uncertainty as

$$U = k \sqrt{u_A^2 + u_B^2} \quad (\text{S2})$$

where u_A and u_B are contributions from, respectively, the type A and type B uncertainty evaluation, and k is the coverage factor. In this work, all the expanded uncertainties are estimated assuming a coverage factor $k = 2$, and all the error bars reported in the figures show a $\pm U$ interval. In the followings, a detailed description of the uncertainty estimation per each relevant quantity is presented.

Distillate flow rate

The flow rate of distilled water (J) consumed by the passive cooler is computed according to equation (2). The associated uncertainty is ascribed to the measurement of the distillate mass variation in the basin (Δm), the duration of the test (Δt , whose uncertainties are evaluated from a uniform probability distribution) and the surface-specific evaporation rate (J_{ev} , whose measurement uncertainty is assumed as normally distributed). Instead, both ρ and A_{net} in equation (2) have negligible uncertainty with respect to the other components. Thus, the combined standard uncertainty is evaluated as

$$u_J = \sqrt{\left(\frac{\partial J}{\partial \Delta m} \frac{u_{\Delta m}}{\sqrt{3}}\right)^2 + \left(\frac{\partial J}{\partial \Delta t} \frac{u_{\Delta t}}{\sqrt{3}}\right)^2 + u_{J_{ev}}^2} \quad (\text{S3})$$

where the half-width contribution to the uncertainty on the distilled water variation and the elapsed time during the test are estimated as $u_{\Delta m} = 3$ g and $u_{\Delta t} = 180$ s, respectively. The surface-specific evaporation rate (J_{ev}) is experimentally evaluated by real-time acquisition of the distilled water weight in the basin when the passive cooler is not operating: the progressively decreasing mass of distilled water over a 3.5 hours test is linearly interpolated, and the uncertainty $u_{J_{ev}}$ evaluated from least square fitting.

Temperature

The temperature drop across the device is estimated considering the average temperatures of the top and bottom surfaces of the prototype, T_T and T_B respectively, as it can be observed in the scheme reported in **Supplementary Fig. S1A**. Thus, $\Delta T = T_T - T_B$. The type A evaluation of the temperature measurement uncertainty is associated with the standard deviation of the N values of T_i temperature measurements at steady state conditions

$$s_{A,T} = \sqrt{\frac{\sum_i^N (T_i - \bar{T})^2}{N - 1}} \quad (\text{S4})$$

Hence, the standard uncertainty for ΔT is estimated considering both the uncertainty contributions of the two sensors used to measure T_T and T_B at steady state conditions, namely

$$u_{A,\Delta T} = \sqrt{s_{A,T_T}^2 + s_{A,T_B}^2} \quad (S5)$$

The measurement uncertainty associated with the thermometric chain (100-Ω PRTs class AA and datalogger) is estimated from the calibration uncertainty of $U_{c,PT} = 0.2$ °C (coverage factor $k = 2$), which has been obtained through four calibration points in the range 20-100 °C. The standard uncertainty associated with the calibration polynomial is evaluated as

$$u_{fit} = \sqrt{\frac{\sum_i^m (T_i - T_{c,i})^2}{m - (p + 1)}} \quad (S6)$$

where T_i is the $i - th$ temperature of the calibration curve, $T_{c,i}$ is the $i - th$ temperature computed through the calibration polynomial, $p = 1$ is the degree of the calibration polynomial and $m = 4$ is the number of calibration points. The measurement uncertainty for each PRT is thus evaluated as

$$u_{B,T} = \sqrt{\left(\frac{U_{c,PT}}{2}\right)^2 + u_{fit}^2} \quad (S7)$$

The uncertainty of ΔT across the cooling device includes the non-uniform temperature distribution in the bottom plate due to the application of two silicone heaters. Thus, the maximum temperature difference across the plate, namely $T_{high} - T_{low}$, is evaluated by two additional 100-Ω PRTs suitably placed to sample the hottest and coldest parts of the evaporator,

as represented in **Supplementary Fig. S1B**. $T_{high} - T_{low}$ is assumed – conservatively – with a triangular distribution, where the width of the interval is increased to include the measurement uncertainty of T_{high} and T_{low} . Therefore, the type B evaluation of the uncertainty related to ΔT is

$$u_{B,\Delta T} = \sqrt{u_{B,T_T}^2 + u_{B,T_B}^2 + \left(\frac{\left(T_{high} + \sqrt{S_{A,T_{high}}^2 + u_{B,T_{high}}^2} \right) - \left(T_{low} - \sqrt{S_{A,T_{low}}^2 + u_{B,T_{low}}^2} \right)}{2\sqrt{6}} \right)^2} \quad (S8)$$

Specific thermal power

The specific thermal power (q) extracted by the cooling device is computed according to equation (1), where both the input thermal load provided by the flat silicone heaters and the thermal losses through the polystyrene insulation are considered. The minimal fluctuations of the voltage (V) and current (I) supplied to the silicone heaters lead to their negligible type A uncertainties; whereas, the resolution of the measuring instruments (*i.e.* voltmeter and amperemeter) leads to a uniformly distributed probability distribution function. Via Ohm's law, the measured voltage and current are considered as correlated. Hence, the standard uncertainty associated with the $Q = IV$ thermal power supplied by the silicone heaters can be estimated as

$$u_Q = \sqrt{\left(\frac{\partial q}{\partial V} \frac{u_V}{2\sqrt{3}} + \frac{\partial q}{\partial I} \frac{u_I}{2\sqrt{3}} \right)^2}, \quad (S9)$$

where $u_I = 10^{-3}$ A and $u_V = 10^{-2}$ V are the amperemeter and voltmeter resolution, respectively.

The uncertainty of the thermal losses is evaluated as

$$u_{Q_L} = \sqrt{\left(\frac{\partial q}{\partial G} u_G\right)^2 + \left(\frac{\partial q}{\partial T_A} u_{T_A}\right)^2 + \left(\frac{\partial q}{\partial T_B} u_{T_B}\right)^2} \quad (\text{S10})$$

where u_G is the standard uncertainty of the thermal conductance of the insulation box (see the following section), $u_{T_A} = 0.5 \text{ }^\circ\text{C}$ is the estimated standard uncertainty of the environment temperature and u_{T_B} is the standard uncertainty on the evaporator temperature, which is evaluated following the procedure described in the previous section. Finally, the combined standard uncertainty on the specific cooling capacity is estimated as $u_q = A_{net}^{-1} \sqrt{u_Q^2 + u_{Q_L}^2}$.

Thermal conductance

The thermal conductance of the insulation box where the cooling device operates is computed as

$$G = \frac{Q}{\Delta T} \quad (\text{S11})$$

where $Q = I V$ is the thermal power supplied by the silicone heaters (powered by I current and V voltage), and $\Delta T = T_F - T_A$ is the difference between the temperature inside the insulation box (T_F) and the environment ($T_A < T_F$). The latter temperatures are both estimated by repeated measurements, considering a measurement interval of 2500 s at steady state conditions. The uncertainty of Q is evaluated according to equation (S9); whereas, the uncertainty of ΔT is

estimated according to equations (S4-S8). Note that the temperature inside the insulation box is evaluated in the closest, middle and farthest point from the heaters. Thus, the uncertainty of the thermal conductance (G_i) of each $i - th$ measurement is evaluated as

$$u_{G_i} = \sqrt{\left(\frac{\partial G}{\partial Q} u_Q\right)^2 + \left(\frac{\partial G}{\partial \Delta T} u_{B,\Delta T}\right)^2} \quad (\text{S12})$$

Four independent measurements of G_i are performed and the associated uncertainties estimated as follows: $(8.5 \pm 0.6) \times 10^{-2} \text{ W K}^{-1}$; $(8.2 \pm 0.8) \times 10^{-2} \text{ W K}^{-1}$; $(8.9 \pm 1.7) \times 10^{-2} \text{ W K}^{-1}$; $(8.5 \pm 0.8) \times 10^{-2} \text{ W K}^{-1}$. The mean value for the thermal conductance is obtained by arithmetic average, while its standard uncertainty is computed as

$$u_G = \sqrt{\frac{\sum_{i=1}^4 u_{G_i}^2}{N^2} + \frac{s_G^2}{N}} \quad (\text{S13})$$

where $N = 4$ is the number of tests performed and s_G the related statistical error.

Membrane permeability

The type B error ($u_{B,K}$) of the membrane permeability measurements described in

Supplementary Note 1 considers both the uncertainty involved in the measured mass flow rate through the membrane (u_j) and the uncertainty provided by the estimated vapour pressure difference during the tests ($u_{\Delta p_v}$). In detail, possible contributions to the uncertainty of the mass flow rate come from the estimation of the water mass measurement uncertainty, namely the

marks on the capillary tube ($u_{tube} = 0.03$ mL) and the uncertainty on the average thickness of water meniscus (u_{men}), which are both considered as uniformly distributed. For each test performed, u_{men} is evaluated by the high-resolution camera as the half-width of the water meniscus. Thus, the uncertainty on the reads of water level in the capillary tube (converted into kg, being ρ the water density) is equal to

$$u_{level} = \frac{\rho(T_A)}{10^6} \sqrt{2 \left(\frac{u_{tube}}{\sqrt{3}} \right)^2 + \left(\frac{u_{men}}{\sqrt{3}} \right)^2} \quad (S14)$$

which, in the assumption of uncorrelated noise in the acquired measures, can be applied to all the water level points collected during each test. Therefore, equation (S14) is used to evaluate the uncertainty of the flow rate across the membrane, that is u_j , via least square fitting. Instead, the vapour pressure difference across the membrane can be computed according to equation (3), depending on the air temperature (T) and water activity coefficients (a) of the two solutions. Since vapour pressure depends on temperature according to the Antoine's law, and the activity coefficients depend on salt concentration (Y), the uncertainty of vapour pressure difference during the tests can be estimated as

$$u_{\Delta p_v} = \sqrt{\left(\left(\frac{\partial p_v}{\partial T_A} (1 - a) - \frac{\partial a}{\partial T_A} \right) u_T \right)^2 + \left(\frac{\partial a}{\partial c} p_v(T_A) \frac{U_{ref}}{2} \right)^2} \quad (S15)$$

where $a = 0.8998$ is the activity coefficient at 170 g L^{-1} salt water dilution computed by equation (5), $u_T = 1 \text{ }^\circ\text{C}$ is the standard uncertainty on the average temperature during the

membrane permeability tests, and $U_{ref} = 2 \text{ g L}^{-1}$ is the expanded uncertainty on salt concentration, obtained by the refractometer specifications. Finally, u_{K_i} of the i -th permeability measurement can be estimated by combining u_J and $u_{\Delta p_v}$ through equation (S2). The final result is obtained averaging the measurements performed, while the related uncertainty can be estimated similarly to equation (S13).

Activity coefficient

The molality of a salt solution can be computed as:

$$m = \frac{Y}{\rho(Y, T) M_s \left(1 - \frac{Y}{\rho(Y, T)}\right)}, \quad (\text{S16})$$

where $\rho(Y, T)$ is the concentration of the solution at a given salt concentration Y and temperature T , and M_s is the molar mass of the solute. The digital refractometer, whose expanded uncertainty is $U_{ref} = 2 \text{ g L}^{-1}$, is used to evaluate the concentration of both NaCl and CaCl₂ solutions, although, in the latter case, the actual concentration is computed by a conversion polynomial evaluated by the linear interpolation of seven calibration points through least square method. Thus, the concentration of a CaCl₂ sample is computed as

$$Y_{CaCl_2} = (0.700 \pm 0.007) Y_{NaCl} + (3.9 \pm 1.3) [\text{g L}^{-1}] \quad (\text{S17})$$

The combined uncertainty on the concentration (u_Y) includes the contributions of the refractometer U_{ref} , the statistical uncertainty evaluated considering five independent

measurements on each sample and, in case of CaCl_2 solutions, the contribution attributable to equation (S17). The activity coefficients are computed according to equation (5), thus their expanded uncertainty is evaluated as

$$U_a = k \sqrt{\left(\frac{\partial a}{\partial Y} s_Y\right)^2 + \left(\frac{\partial a}{\partial T} u_T\right)^2} \quad (\text{S18})$$

where $u_T = 1 \text{ }^\circ\text{C}$ is the standard uncertainty of the room temperature.

Note S3. Solute transport through the condensing side

In the current implementation of the cooler prototype, all condensing layers have fixed volumes; hence, due to the water flux coming from the evaporators, the total hydraulic pressure rise induces a concurrent mass flux from the condenser to the upper reservoir. However, in general, there is no guarantee that the natural (solute) mass transfer from the high salinity reservoir to the lower salinity condenser is effective to keep up with the rate/pace at which the condenser water is diluted. Hence, a concentration dilution in time of the salty solution initially present in the condensing layers might happen thus causing a decrease in the device performance. However, the device could be properly designed in order to ensure an effective solute transport from the reservoir to the condenser even in the presence of only natural phenomena. In order to support this, we report here below some natural mass transfer estimates.

By referring to **Supplementary Fig. S3**, we notice that a first natural transport of solute molecules from the upper boundary of the condenser downward is driven by a density difference ($\Delta\rho$) within the condenser itself (induced by a salinity difference equal to 170 g L^{-1}). The associate mass flux can be estimated as

$$\dot{m} \approx \frac{\text{Sh} \cdot D}{L} \cdot \Delta\rho = \frac{\text{Sh} \cdot 2 \cdot 10^{-9}}{2 \cdot 10^{-3}} \cdot 150 \approx \text{Sh} \cdot 5.4 \cdot 10^{-1} \frac{\text{kg}}{\text{m}^2\text{h}} \quad (\text{S19})$$

where Sh , D , L are the Sherwood number, the diffusion coefficient and the transport length, respectively. Hence, it follows that, even in a very conservative scenario (*i.e.* purely diffusive regime with $\text{Sh} \approx 1$), we observe a sufficient solute flux ($0.54 \text{ kg m}^{-2}\text{h}^{-1}$) as compared to the water one in each stage. As a result, the first transport in the condenser does not represent a critical bottleneck for the device performance.

At the same time, an effective natural transport of the solute from the high-salinity reservoir to the condenser has to happen through the connection tube (see **Supplementary Fig. S3**). In order to fix ideas, let us estimate the salinity value in the condenser after one working hour. This value is evaluated by considering the distillate water consumption of each stage (*i.e.* $\approx 0.6 \text{ L m}^{-2}\text{h}^{-1}$) and the mass balance equation. The resulting salinity is equal to 116 g L^{-1} . As such, the solute transport from the top downwards becomes similar to free heat convection in a cavity heated from below. In the latter (thermal) situation, for liquids, the Globe-Dropkin relationship (41) holds

$$\text{Nu} = 0.069 \cdot \text{Gr}^{\frac{1}{3}} \cdot \text{Pr}^{0.407} \quad (\text{S20})$$

with Nu, Gr, Pr being the Nusselt, Grashof and Prandtl numbers, respectively. The above relationship can be converted in a mass transfer one by resorting, for instance, to the following Chilton-Colburn analogy (42) between heat and mass transfer phenomena

$$\frac{\text{Sh}}{\text{Nu}} = \frac{\alpha}{D} \left(\frac{\text{Pr}}{\text{Sc}} \right)^{2/3} \quad (\text{S21})$$

with α , Sc being thermal diffusivity and Schmidt number. In our case, we can estimate the following solutal Grashof number

$$\text{Gr} = \frac{g \cdot \Delta\rho/\rho_0 \cdot h^3}{\nu^2} \approx \frac{9.81 \cdot 0.037 \cdot (5 \cdot 10^{-2})^3}{10^{-12}} \approx 4.55 \cdot 10^7 \quad (\text{S22})$$

with g, ν being the gravitational acceleration and kinematic viscosity. By means of the above Globe-Dropkin relationship, we can estimate a Nusselt number of $\text{Nu} \approx 51.4$, which – according to the above Chilton-Colburn analogy – corresponds to a Sherwood number of

$$\text{Sh} \approx 51.4 \cdot \frac{\alpha}{D} \left(\frac{\text{Pr}}{\text{Sc}} \right)^{2/3} = 51.4 \cdot \frac{1.55 \cdot 10^{-7}}{2 \cdot 10^{-9}} \cdot \left(\frac{6}{500} \right)^{2/3} = 207 \quad (\text{S23})$$

where properties of salty solutions have been evaluated according to the data reported in the library from ref. (43) and in the work by Winter (44). It follows a mass flux of

$$\dot{m} \approx \frac{\text{Sh} \cdot D}{L} \cdot \Delta\rho = \frac{207 \cdot 2 \cdot 10^{-9}}{5 \cdot 10^{-2}} \cdot 54 = 1.6 \frac{\text{kg}}{\text{m}^2\text{h}} \quad (\text{S24})$$

In the present configuration, due to a very small tube section area A connecting the reservoir with the condenser in the order of $A \sim O(10^{-5} - 10^{-4}) \text{ m}^2$, the mass flow rate is clearly not able to keep up with the dilution mass rate of zero-salinity water coming from the evaporator (in the order of $\sim O(10^{-1}) \text{ kg m}^{-2}\text{h}^{-1}$). This explains the performance drop after a sufficiently long time. However, this is due to a sub-optimal engineering design of the reported device, which, in future up-scaled prototypes, can be re-designed in order to properly ensure a sufficient mass transfer of the solute from the reservoir to the condensers.

In this respect, we notice that it is possible to enhance orders of magnitude the natural mass transport induced by salinity gradients thanks to the corresponding gradients in surface tension, if between the condenser and the high-salinity reservoir a proper wick is present (air-salt water interface). In this case, it has been proven that the difference in surface tension results in a Marangoni convection that can be effectively described using a much higher apparent diffusion coefficient D_{app} . This apparent coefficient can exceed the molecular one ($D = 2 \cdot 10^{-9} \text{ m}^2\text{s}^{-1}$) up to $D_{app}/D \sim O(10^4)$ (see Fig. 2b in ref. (45)). In our specific case, for the same wick that we use in the evaporator, we have estimated by finite elements simulations $D_{app} \sim 10^{-5} \text{ m}^2\text{s}^{-1}$ in a configuration where the salinity difference is imposed between 170 and 116 g L^{-1} (46). As a result, in this case, a rough estimate of the mass flux is in the order

$$\text{Sh} \approx \frac{\alpha}{D} \left(\frac{\text{Pr}}{\text{Sc}} \right)^{\frac{2}{3}} \cdot \text{Nu} = \frac{1.55 \cdot 10^{-7}}{10^{-5}} \cdot \left(\frac{6}{0.1} \right)^{\frac{2}{3}} \cdot 51.4 = 12.36 \quad (\text{S25})$$

which yields

$$\dot{m} \approx \frac{\text{Sh} \cdot D}{L} \cdot \Delta\rho = \frac{12.36 \cdot 10^{-5}}{5 \cdot 10^{-2}} \cdot 42 \cong 445.58 \frac{\text{kg}}{\text{m}^2\text{h}} \quad (\text{S26})$$

Assuming a 2-mm-thick wick exiting a 1 m × 1 m condenser from one of the edges, the cross section will be $A = 2 \cdot 10^{-3} \text{ m}^2$, which yields a mass flow rate of

$$\dot{m} \cdot A \approx 0.75 \frac{\text{kg}}{\text{h}} \quad (\text{S27})$$

in a 1 m² device. This value is indeed sufficient to prevent dilution of water in the condenser, since the vapour flux in each stage is in the order of $\sim O(10^{-1}) \text{ kg m}^{-2}\text{h}^{-1}$.

Note S4. Exergy analysis of the passive cooler

The exergy analysis of the passive cooler has been carried out. The dead state is defined by the following quantities: $T_0 = 30 \text{ }^\circ\text{C}$; $p_0 = 1 \text{ bar}$; molar fraction $x_0 = 0.1$ (*i.e.* 170 g L⁻¹ salinity in the condenser). The exergy equation for the cooler (in stationary conditions and incompressible fluid flow) can be written as

$$\Psi_{in} = -G_{in}b_{in} + \Psi_{irr} \quad (\text{S28})$$

where Ψ_{in} is the inlet thermal exergy flux equal to the thermal flux extracted from the cold chamber multiplied by the Carnot factor; G_{in} represents the mass flow rate that enters the device (equal to the distillate water consumption); b_{in} is the total specific flow exergy and Ψ_{irr} the exergy destruction within the system. Then, the above equation can be re-written as

$$Q_{in} \left(1 - \frac{T_0}{T_{in}}\right) = -G_{in}RT_0 \ln\left(\frac{1}{1-x_0}\right) + \Psi_{irr}. \quad (\text{S29})$$

Note that the thermal exergy flux that exits the last condenser $Q_{out} \left(1 - \frac{T_0}{T_{out}}\right)$ is null, since Q_{out} is rejected at ambient temperature. The flow exergy content related to G_{out} is also null, because of the choice of the dead state. The Second Law efficiency of the cooler is thus evaluated as

$$\eta_{II} = \frac{\Psi_{in}}{G_{in}b_{in}} \quad (\text{S30})$$

Results of this exergy analysis in case of a 1-, 4- and 10-stages configurations of the cooler are summarized in the **Supplementary Tab. S2**.

Note S5. Comparison with other passive cooling approaches

Adiabatic evaporative passive cooling

The popular adiabatic evaporative cooling is one of the simplest non-cyclical passive cooling approaches. It is well-known, though, that the maximum temperature difference and the maximum achievable cooling load are both strongly dependent on the intermittent value of the atmospheric relative humidity, with vanishing performance at nearly saturation conditions. It follows that evaporative cooling may be not effective in regions with very high humidity levels (e.g. tropical and sub-tropical regions). On the contrary, a system exploiting salinity differences is not affected at all by the atmospheric humidity value. To fix ideas, let us consider the average summer conditions in Dubai, where temperatures can be in the order of 40 °C and the relative humidity about 90% during the summer season (see e.g. <https://www.dubai.com/v/geography/>). Under those conditions, an estimate of the maximum temperature difference achievable at moist air saturation is given by the Carrier diagram, where the maximum temperature differences of 1 and 2 °C correspond to a relative humidity of 90% and 80%, respectively. On the other hand, the water evaporation rate through a surface S can be estimated by

$$\dot{m}_{H_2O} = h_m S (\rho_{sat} - \rho) = h_m S M_{H_2O} \frac{(p_{sat}(T) - p)}{RT} \quad (S31)$$

with h_m , M_{H_2O} and p being the convective mass transfer coefficient, the molar weight of water and the water vapour pressure in air, respectively. Note that p_{sat} refers to the saturation pressure of water vapour at given T . In passive systems, the typical natural convective mass transfer phenomena can be characterized by Sherwood numbers (Sh) in the order of (47) $10 < Sh < 80$.

To fix ideas, let us consider a (1 m x 1 m) evaporating surface. In this case, the maximum convective mass transfer coefficient can be obtained with $Sh = 80$, namely

$$h_m = \frac{D_{H_2O} Sh}{L} = 2.3 \cdot 10^{-3} \frac{m}{s} \quad (S32)$$

where D_{H_2O} is the diffusivity of water and L the characteristic length. Therefore, the specific water evaporation flux at $T = 40$ °C and relative humidity $\varphi = 0.8$ can be estimated as

$$\frac{\dot{m}_{H_2O}}{S} = h_m M_{H_2O} p_{sat}(T) \frac{(1 - \varphi)}{RT} = 2.35 \cdot 10^{-5} \frac{kg}{s m^2} \quad (S33)$$

whereas, the specific water flux is even half for a relative humidity value of $\varphi = 0.9$. Therefore, the cooling load can be at the best (*i.e.* for the highest Sherwood number)

$$\begin{aligned} \phi_{\varphi=80\%} &= \frac{\dot{m}_{H_2O}}{S} \Delta h \approx 58 \frac{W}{m^2} \\ \phi_{\varphi=90\%} &= \frac{\dot{m}_{H_2O}}{S} \Delta h \approx 29 \frac{W}{m^2} \end{aligned} \quad (S34)$$

being Δh the enthalpy of evaporation of water. We notice that the above estimates are optimistic because they do not include “parasitic” convective heat transfer towards the environment due to the unavoidable coupling of convective mass and heat transfer phenomena, where the higher the Sherwood the higher the Nusselt number. This will reduce further the net cooling flux at least by a factor 5-10 $W m^{-2} K^{-1}$, which is a typical convective heat transfer coefficient for air under natural convection regime (48). Nevertheless, the above estimates of cooling capacity are 3 to 6 times lower than the ones obtained in our experiments (see **Fig. 4**).

Daytime radiative passive cooling

Similarly to the adiabatic evaporative cooling, also the daytime radiative cooling is heavily hindered in case of high humidity in the atmosphere, as the transparency of the infrared atmospheric window may be significantly reduced. This point has been discussed in the manuscript. More specifically, the ruling parameter here is the so called “Precipitable Water Vapour - PWV”, which is expressed in millimetres and represents the depth of water that would result if all the vapour in a column of the atmosphere above a certain location was condensed as rain. As discussed in ref. (49), important daytime cooling can be accomplished for dry environments (*i.e.* PWV in the order of 1-10 mm), where the sky window opens not only at wavelengths of 8-13 microns (first window) but also within 16-25 microns (second window) (11, 36). On the other hand, warm regions can be characterized by $PWV > 20$ mm (50), where the second window is almost completely closed and the first one less transparent. Under the latter conditions, a sub-ambient daytime cooling might not even be achievable and only a cooling above the ambient temperature is possible (49). Conversely, the passive cooler discussed in this article is not sensitive to the ambient humidity level, since the cooling capacity is generated by a salinity difference. A comprehensive comparison between the cooling capacity of daytime radiative cooling devices and our results is reported in **Fig. 4**.

Seasonal ice storage

Ice collection for seasonal storage is also possible and indeed effective for reaching low temperature and significant cooling load. However, this is only possible in some specific regions. For instance, we are only aware of one popular case, namely the air conditioning of the Hungarian parliament building in Budapest owing to the ice collection from lake Balaton during the winter season (51). Clearly, this approach can be implemented only under very specific geographical conditions, namely a lake that undergoes freezing close to a region with significant cooling needs during summer. What we propose, although characterized by smaller temperature differences and cooling loads, has the ambition to be more generally applicable, not only because of the possible cyclic operation mode (if combined with a solar regenerator), but also because of the significantly increasing brine production from new desalination plants. In this respect, it suffices to notice the impressive increase in the worldwide desalination capacity (and consequently brine production), which has more than doubled in ten years (2005-2015) (52).

Note S6. Details on the coupling between passive distiller and cooler

To achieve a suitable regeneration of the salinity difference in each cooling stage and thus a steady cooling cycle, the coupled distiller has to produce a suitable mass flow rate of distillate. To enhance the distillate productivity of the passive distiller considered in this work (19), two ways can be envisioned. First, a high-temperature heat source can be exploited. However, to keep the physical/chemical stability of the hydrophobic membrane and to prevent/limit scaling in the distiller, lower temperatures are preferable. In detail, as commonly done in case of membrane distillation processes, the maximum operating temperature should not exceed 80 °C. The second

way to improve the potential regeneration capabilities of the passive distiller is to increase the ratio between the area of the distiller and the cooler (see **Fig. 5C**).

We carried out computations to estimate the ratio between the areas of the two devices ($A_{Distiller}/A_{Cooler}$, see **Supplementary Fig. S9**) as function of the concentration of the feed solution (see the activity a in **Supplementary Fig. S9**). In case of high-salinity brines (*i.e.* lower activity), $A_{Distiller}/A_{Cooler}$ should increase to counterbalance the performance decrease of the distiller (lower driving force and, thus, J_D) and the larger consumption of the cooler (higher driving force). In detail, in case of $a = 0.75$, a ratio $A_D A_C^{-1}$ equal to 3.7 must be ensured to avoid dilution and thus an unsteady cooling cycle.

Note S7. Coefficient of performance

The Coefficient Of Performance (COP) of the passive solar cooling system realized by coupling the passive cooler and distiller (see **Fig. 5A**) can be computed as (53)

$$\text{COP} = \frac{q A_{Cooler}}{q_{sun} A_{Distiller}} = \frac{q}{q_{sun}} \frac{1}{R_A}, \quad (\text{S35})$$

being q and A_{Cooler} the specific cooling capacity and active surface of the cooler, respectively; q_{sun} the solar irradiance and $A_{Distiller}$ the surface of distiller exposed to the sun. Since q_{sun} depends only on the installation site, q should be maximized and R_A minimized to optimize the COP of the system. Clearly, these quantities are highly sensible to the different configurations

(e.g. number and stratigraphy of the cooling/distillation stages) and operating conditions (e.g. ambient temperature, type and concentration of the solution) of both cooler and distiller in the coupled system.

For illustrative purposes, we compute the COP of the passive solar cooling system reported in **Fig. 5**, namely:

- Cooler with $N_{Cooler} = 4$ number of stages and stratigraphy equal to the one tested in the experiments.
- Distiller with $N_{Distiller} = R_S N_{Cooler}$ number of stages and optimized stratigraphy (0.5 mm air gap; membrane with 3.0 μm pores).
- Operating fluids: distilled water and NaCl-water solution at 170 g L⁻¹ concentration.
- Ambient temperature equal to 30 °C, $q_{sun} = 1000 \text{ W m}^{-2}$.

Furthermore, $R_S = 2.5$ and thus $N_{Distiller} = 10$ is the maximum number of distillation stages that could be practically implemented with the current design of the passive distiller (19). Under these assumptions, **Fig. 5C** shows that the highest cooling performance of the solar-driven system can be obtained with $R_S = 2.5$, $q = 100 \text{ W m}^{-2}$ and thus $R_A = 0.6$, namely COP = 0.17.

A more in-depth optimization of both distiller/cooler configuration and operating conditions could further increase this COP value, which has been computed only for illustrative purposes on a sub-optimal system. For instance, static solar concentration technologies (e.g. Fresnel lens) could easily further reduce R_A : in this way, in case of an optical concentration equal to 2, the COP could roughly double, that is COP = 0.34, while keeping the overall system passive. These COP values – obtained from a completely passive solar system operating with a sustainable and

non-toxic solution – seems to be not far from well-established, industrialized and active technologies. In fact, active solar cooling systems based on adsorption cycles show typically $COP = 0.05 - 0.5$; whereas, systems based on single-effect absorption cycles $COP = 0.35 - 0.85$ (53, 54).

Note S8. Coupling with high-salinity brines produced by different desalination technologies

The presented cooling system can be operated either as a component of a cyclic machine, or with a net consumption of fresh and salty water. Some of the areas with cooling needs can also present water scarcity issues, where it only makes sense to operate the system in a cyclic mode. However, there are important exceptions where both cooling needs and abundant salinity differences are either naturally available (e.g. nearby salt mines or salt-works) or coming from brines produced in large desalination plants. In the latter cases, in our system the condensers could be fed by high-salinity solutions (*i.e.* brines), whereas seawater (with lower salinity) could be adopted at the evaporators. Following this approach, no fresh water would be needed whatsoever. We also notice that, the direct discharge of hypersaline concentrate water (e.g. brines from desalination plants) into the sea is a serious environmental and economic problem that is drawing an increasing attention in the scientific community. In order to fix ideas on the relevance of the situations mentioned above, in ref. (55), authors estimate a total production of 142 million m^3 per day of brine, with Saudi Arabia, UAE, Kuwait and Qatar accounting for 55% of the total share. We also notice that the latter Countries are known to have impressive cooling needs. According to ref. (56), over 70% of electricity consumption in Saudi Arabia is used for air conditioning and cooling.

Let us consider an illustrative case where the condensers of our cooler could be fed by the brine produced from a desalination plant. The typical concentration range of total dissolved solids (TDS) of brines produced by reverse osmosis is 70 to 80 g L⁻¹ (26). Currently, several concentration technologies, ranging from solar ponds to electrodialysis, are employed to increase the recovery rate of desalination plants, in order to reduce the environmental impact of high-salinity brines and ease their disposal. In particular: mechanical vapour compression can be used to reach a TDS concentration of 250 g L⁻¹ (57); forward osmosis allows to reach concentrations ranging from 180 g L⁻¹ (58) up to 220 g L⁻¹ (59); vacuum membrane distillation has been recently proved to achieve TDS concentrations in the range 150–300 g L⁻¹ (59-61). The dashed blue line in **Supplementary Fig. S15** shows the characteristic curve of the passive cooler with seawater in the evaporators (35 g L⁻¹, 0.6 molal) and brine in the condensers (220 g L⁻¹, 4.1 molal), whilst the dotted black line exploits the typical reverse osmosis brine (80 g L⁻¹, 1.4 molal) in the condensers. Clearly, these operating conditions would not consume any distilled water. For reference, **Supplementary Fig. S15** also reports the characteristic curve experimentally validated in the present work (solid red line), where a salt solution fed the condensers (170 g L⁻¹, 3.1 molal) and distilled water the evaporators.

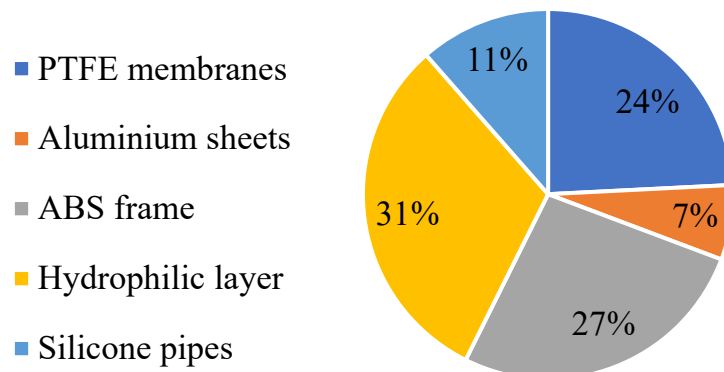
Note S9. Cost analysis of the laboratory-scale prototypes

Passive cooler

Here, a brief cost analysis of the tested lab-scale prototype is reported. The prototype cost has not been optimized and, due to its small size, it does not exploit any economy of scales yet. The

optimization of the cost in a possible industrial scenario is beyond the scope of this work, in which we focused mostly on the proof of concept. The **Supplementary Tab. S3** lists the unitary cost of the materials employed, the quantity needed for one cooling stage and the considered supplier. Whenever possible, the wholesale cost of the material is considered. Note that the considered area of hydrophilic layer also includes the scraps required for shaping the supply stripe, and that the cost of the sealing silicone is negligible. Hence, the overall cost of one cooling stage is approximately equal to 1.9 €. The following pie chart shows the percent cost splitting for a single stage.

Cost splitting of materials needed in a single stage of the proposed passive cooling device



Finally, four nuts and bolts and one additional aluminium plate should be used to assemble the 4-stage prototype, with an additional cost of 0.9 €. The forced convection heat sink used during the experiments has an approximate cost of 15 €, but this may change according to each specific application (*i.e.* it might be replaced by a natural convection heat sink).

Passive distiller

A cost estimation for the passive distiller considered in the assessment of the solar cooling cycle in **Fig. 5** is then provided. This cost estimation relies on the prototype extensively tested in laboratory and field conditions detailed in ref. (19). The **Supplementary Tab. S4** lists the unitary cost of the materials employed, the quantity needed for one distillation stage and the considered supplier. Whenever possible, the wholesale cost of the material is considered. Note that the considered area of hydrophilic layer also includes the scraps required for shaping the supply stripe. For example, a distillation stage with an active surface equal to the one of the tested cooler (*i.e.* 13 x 13 cm²) has a cost approximately equal to 1 €. If a multistage assembly of the passive distiller is considered, the cost of the convection reducer (50 €/m², wholesale), selective solar absorber (5.3 €/m², wholesale) and heat sink for natural convection (227 €/m², *RS Components*) should be included as well. As a result, a 4-stage prototype of passive distiller with 13 x 13 cm² surface exposed to the sun would cost approximately 9 €. Note that, in a complete solar cooling cycle, the salt and distilled water basins would be shared between the distiller and cooler, thus not constituting additional costs for the distillation side.

Note S10. Considerations on environmental and life-cycle analysis issues of the passive cooler

The passive cooler discussed in the article is made of the following materials: stainless steel (bolts and nuts); aluminium (separation plates, heat sink); acrylonitrile butadiene styrene (ABS, structural frame of each cooling stage); polytetrafluoroethylene (PTFE, membranes); microfiber (hydrophilic layers). Steel and aluminium parts are fully recyclable and, to this purpose, efficient

recycling processes and facilities are well established worldwide (e.g. 34.3% of all metal wastes have been recycled in the US in 2015 (62)). Both ABS and PTFE are thermoplastic and can be recycled, even though their purity would tend to degrade with each reuse cycle (63-65). The employed microfiber, instead, is made of 70% viscose (regenerated cellulose fibre), 18% polypropylene and 12% polyester that, despite being partially recyclable, could be a source of microplastic accumulation in marine habitats (66). Furthermore, the tested assembly is only a lab-scale prototype and for simplicity it contains some epoxy sealant and silicone (for making the plastic frames waterproofed) that are not recyclable at all. Although not in the scope of the present work, in the near future, the environmental impact of the device could be further reduced by substituting the most critical materials, namely the microfiber and sealants. For example, the hydrophilic layer could be made of natural fibres; whereas, the ABS frame (which is now treated by epoxy and silicone to become waterproofed) could be made of aluminium or stainless steel.

Regarding the presence of a high-salinity solution in the condensers, the passive cooler could be envisioned as a device synergic with desalination plants for mitigating their brine discharge issues. In fact, discharging the produced brine in a cost-effective and eco-friendly way still remains a serious challenge in desalination plants (67). The most common brine disposal methods are surface water discharge or injection into saline aquifers, both presenting serious environmental risks if intensively exploited. In fact, the discharge of high-salinity solutions into the sea is a major threat to marine ecosystems, particularly to seagrasses such as the *Posidonia Oceanica* (68, 69); whereas, the injection into confined salt water aquifers, despite being largely used for brackish water desalination, may cause contamination of the overlying potable aquifers due to underground connections or leakages (70, 71). To mitigate the previous issues, brine

should be diluted before being discharged into the receiving water body (72). However, the brine dilution can be particularly challenging in large desalination plants, where the mass flow rate of brine is substantial and localized in a limited coastal area (e.g. Gulf nations) (55). In this context, our cooling device would have no additional brine production, in case of both cyclic and non-cyclic operations. On the one hand, the cyclic distiller-cooler assembly (see **Fig. 5**) would not involve any brine disposal into the environment. On the other hand, if the passive cooler operates with a net consumption of low-salinity (e.g. seawater) and high-salinity (e.g. brine) water solutions, the final result would be the dilution of the brine from desalination plants before their final discharge into the environment.

Note S11. Cooling performance of the device under the sun

Let us assume that the proposed cooling device is used in a non-cyclical configuration with a net consumption of fresh water (*i.e.* without salt water regeneration). Clearly, if this is not the case, the regeneration device will protect the upper surface of the cooler from solar radiation. Under those operating conditions, we envision that the cooling device can be able to properly function if its top surface is effectively shielded from solar radiation and does not differs too much from the (lower) building temperature.

To fix ideas, let us focus on the **Supplementary Fig. S10**, where we imagine having a solar shield made of a good thermal insulator (e.g. expanded polystyrene) covered at both ends by highly reflective layers (e.g. the VEGA energy by Almedco, with overall optical reflection > 0.92). As visible in the **Supplementary Fig. S10**, we assume that a sufficiently large air gap

between the solar shield and the cooling device is present, where forced air (at ambient conditions) can circulate. To estimate the temperature difference between the top cooler surface and the ambient (here assumed to be 30 °C), we implemented the simple one-dimensional model schematically reported on the right-hand side of **Supplementary Fig. S10** by means of the package SIMSCAPE available in Matlab (see **Supplementary Fig. S11**).

In the right-most column of the **Supplementary Tab. S5**, we report the computations of the temperature increase of the top cooler surface with respect to the ambient under various operating conditions. As far as solar reflectance is concerned, we assumed the value of commercially available materials. The value of the cooler flux is chosen according to minimum and maximum measured cooling capacities of the presented device for CaCl₂-water solutions. Advection coefficients are chosen by assuming typical values for natural advection on the solar shield and forced convection in the air gap (73). Top and bottom surfaces in the air gap are assumed finned with a double exchange area (as compared to the planar area).

On the one hand, results in the **Supplementary Tab. S5** show that it is relatively easy to limit the temperature increase (with respect to ambient) due to solar radiation by a proper combination of solar reflectance layers and insulating materials for the sun shield. On the other hand, it is clear that the critical parameter for ensuring sub-ambient cooling is represented by the advection coefficient on the top surface of the cooling device. In other words, especially at high fluxes q_{cond} , sub-ambient cooling is possible in the presence of an effective forced advection, removing the heat from the top condenser. Under the assumption that the building temperature is not too cold as compared to ambient, practical applications of the suggested device can be envisioned.

Note S12. Durability and corrosion of the passive cooler

The cooler prototype was built in February 2018 and has been used continuously during the experimental campaign, which lasted until November 2018. The device did not report any significant wear and the silicone sealing never leaked during the months of usage. During the loading process, the overpressure in the stages slightly deformed the hydrophobic membranes. Thus, the membranes were replaced after 4 months of usage (before assessing the performance with the calcium chloride dilution), to avoid a possible bias of observed results.

The salt dilutions are in direct contact with corrosion resistant polymeric materials (*i.e.* silicone pipes and sealant, PTFE membranes, plastic frame) and aluminium. In particular, the frame is built by fused material deposition technique using ABS plastic and then made waterproofed by Nano-Seal 180W. The data sheet of this sealant reports a good grade of resistance to corrosion: in fact, the frame was not damaged by the sodium chloride and calcium chloride solutions during the whole experimental campaign. However, other specifically designed sealants could grant even higher resistance to corrosion, e.g. the Nano-Seal STR. Notice that, after 9 months of usage, the aluminium plates developed only an opaque veneer.

Note S13. Boundary effects on the temperature field in the evaporator

The distilled and salt water supplied respectively to each evaporator and condenser are in thermal equilibrium with the environment (namely, $T = 30\text{ }^{\circ}\text{C}$). Indeed, this could have negative effects on the temperature drops across each single stage due to boundary effects.

To quantify this effect, we have estimated the boundary disturbance by a representative COMSOL Multiphysics stationary simulation. This phenomenon is studied by considering the hydrophilic layer (evaporator; size: $13 \times 13 \times 0.1\text{ cm}^3$, see **Supplementary Fig. S14**), because of its lower i) temperature (with respect to the ambient/condenser) and ii) heat capacity (with respect to the cavity of the condenser). The following boundary conditions have been applied: i) fixed temperature drop across the evaporator equal to $3\text{ }^{\circ}\text{C}$ ($T_{top\ surface} = 30\text{ }^{\circ}\text{C}$); ii) purely conductive heat transfer (because of the low velocity of water, namely 10^{-7} m s^{-1} , due to capillary action); iii) fixed temperature ($T_{freshwater} = 30\text{ }^{\circ}\text{C}$) at the border at which freshwater enters the control volume through the 3 cm strip.

As depicted in the **Supplementary Fig. S14**, the temperature disturbance does not exceed 2 mm from the inlet boundary. This boundary effect is thus negligible, mainly because of the reduced extension of the strips through which the freshwater reaches each evaporator (only 3 cm over the total 13 cm side are used to supply freshwater; furthermore, the water feeding takes place only from one side of the evaporator). In conclusion, the one-dimensional heat transfer model described in the main text can be considered as a sufficiently accurate and reliable approximation.

Supplementary Figures

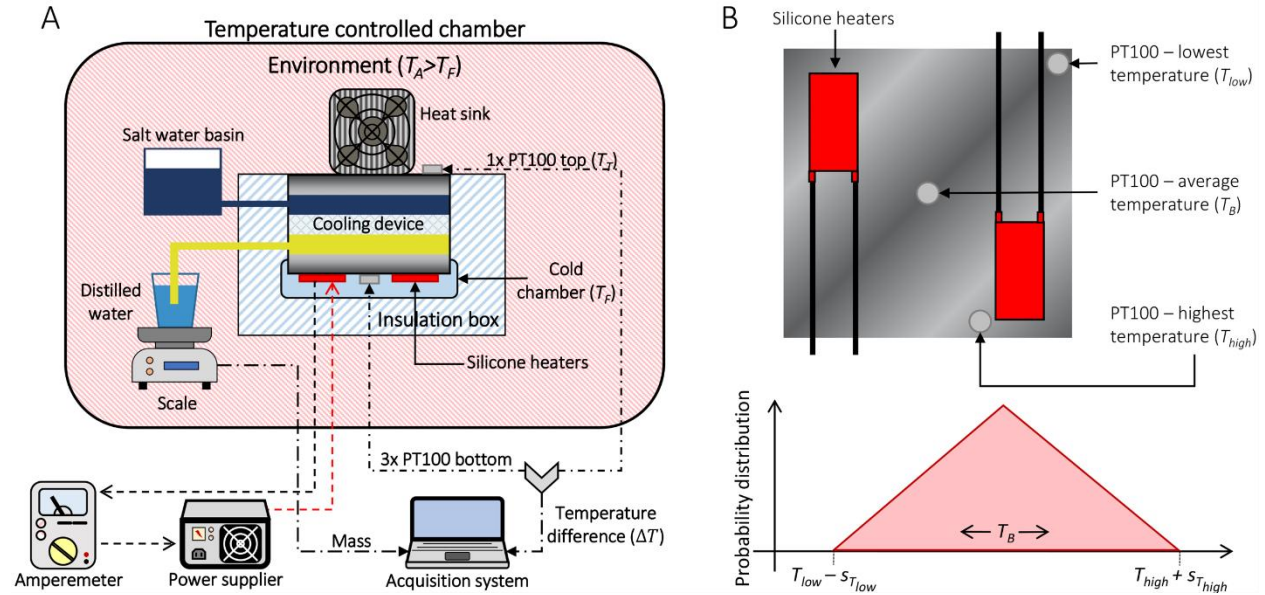


Fig. S1. Experimental setup to measure cooling capacity. (A) Schematic of the experimental setup adopted to assess the cooling capacity of the passive cooler. The cooling device, which is enclosed in a polystyrene box to minimize thermal losses with the environment, is tested in an ambient at controlled temperature. For the sake of simplicity, only a single stage of the cooling device has been represented here. Two silicone heaters – connected to a power supplier and enclosed in the insulation box as well – are attached to the lowermost surface of the cooler (*i.e.* the first-stage evaporator) and provide it a constant thermal load. The passive cooler extracts the thermal power from the silicone heaters and discharges it in the environment through the upper heat sink, which is attached to the last-stage condenser and operates by forced convection. The acquisition system is employed to measure the temperature difference across the device (ΔT) and the weight (m) of distilled water in the basin, which progressively decreases with time as it is consumed by the passive cooler. (B) Schematic of the positioning of the silicone heaters and the

three thermo-resistances on the first-stage evaporator of the device. The highest and lowest temperatures measured on the plate, namely T_{low} and T_{high} , and their uncertainties are used to evaluate the uncertainty of the average plate temperature (T_B) as explained in **Supplementary Note 2**.

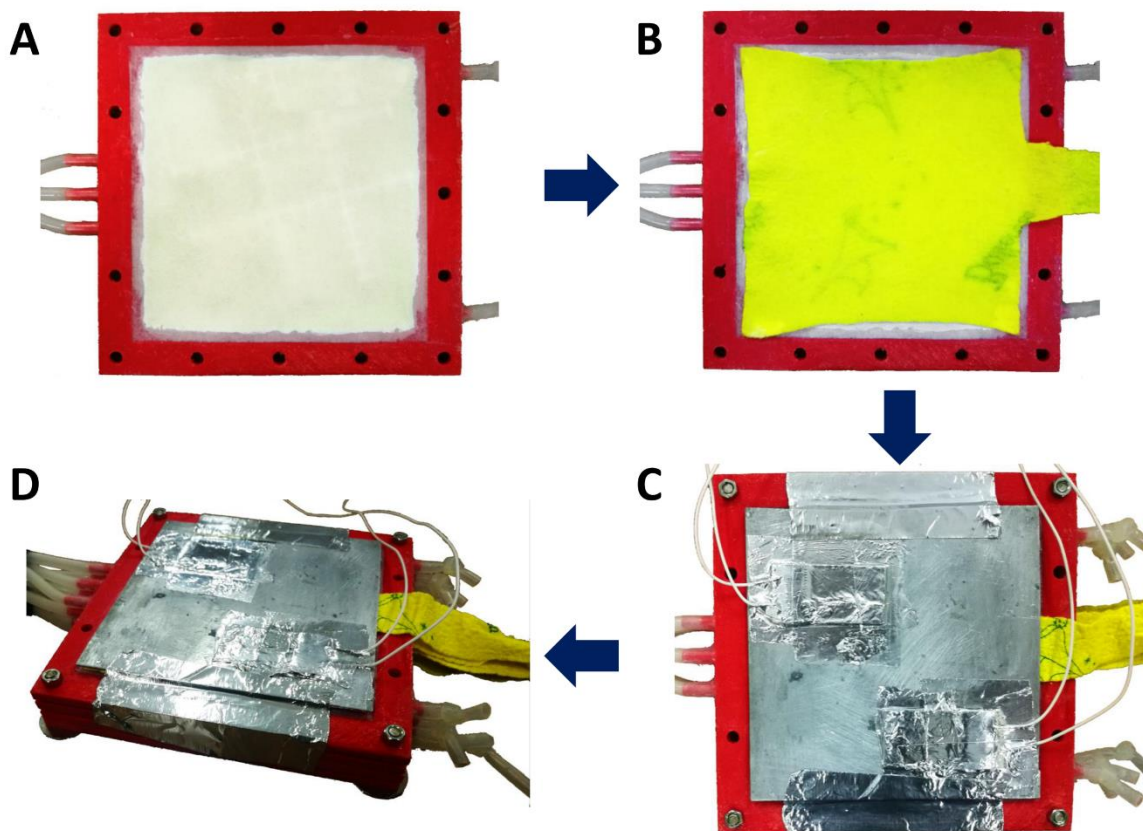


Fig. S2. Assembly of the passive cooling device. The main components of the tested prototype of cooler and the assembly process are presented. (A) In the figure, we report the assembly of the first stage of cooler, which is in contact with the silicone heaters. The plastic frame (red, acrylonitrile butadiene styrene) supporting the membrane (white, polytetrafluoroethylene with pore size $1.0 \mu\text{m}$ and thickness approximately 0.1 mm) is shown. On the top side of the

membrane (*i.e.* first-stage condenser), salt water is supplied through three plastic tubes, which can be seen on the left-hand side of the plastic frame; on the bottom side of the membrane (*i.e.* first-stage evaporator), distilled water is supplied through **(B)** a hydrophilic layer (yellow, microfibre). **(C)** A rigid plate (grey, aluminium) separates the first-stage evaporator from the two silicone heaters. **(D)** Picture of the assembled 4-stage cooling device, where the first stage is still visible at the top. Photo Credit: Matteo Alberghini, Politecnico di Torino.

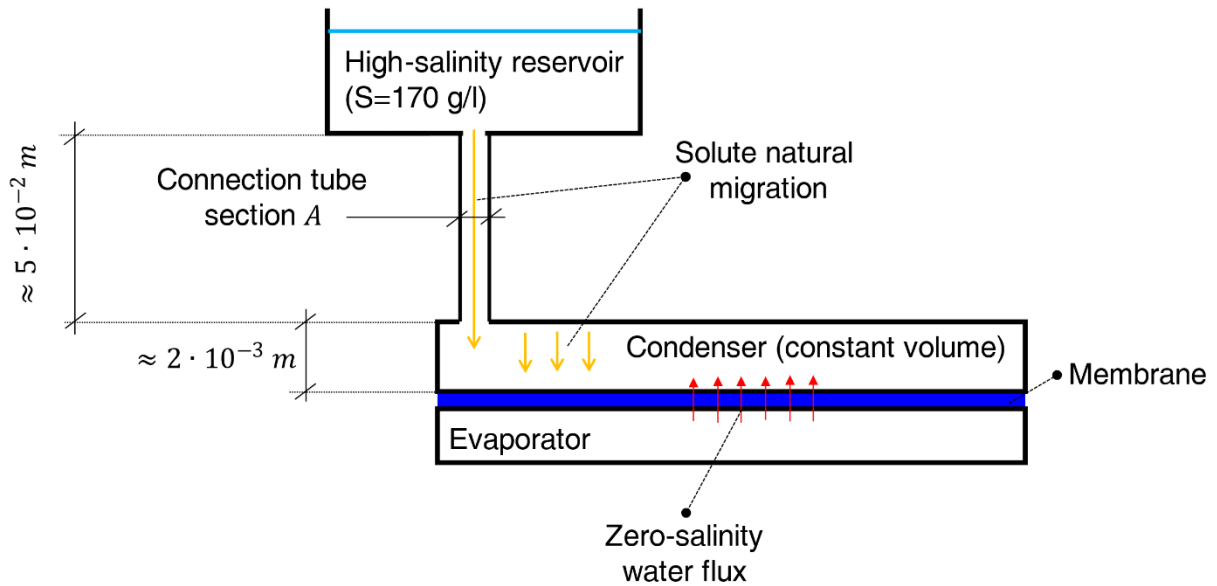


Fig. S3. Natural mass transport phenomena in the present passive cooler. The mass transport of water and salt in the static/passive configuration of the presented cooler relies on natural/spontaneous transport phenomena only, in order to get rid of mechanical components with moving parts. The **Supplementary Note 3** reports an estimate of the solute transport through the connection tube and the condenser volume, with some speculations on possible strategies to enhance the solute transport via the Marangoni effect.

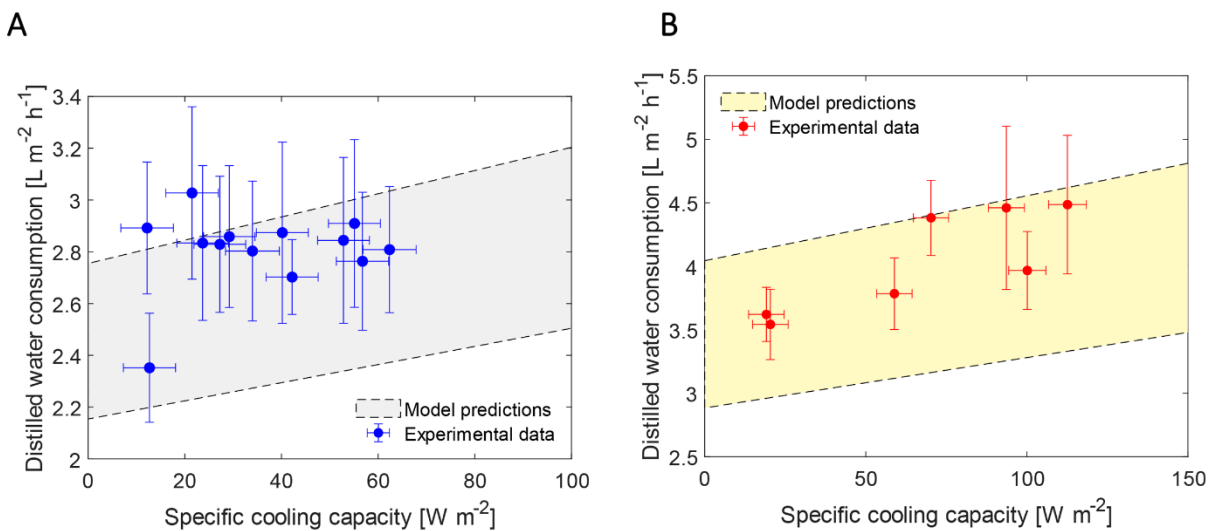


Fig. S4. Distillate consumption by the passive cooler. Experimental results and modelling predictions of the distilled water consumption by the passive cooling device during laboratory tests, considering 3.1 molal (A) NaCl and (B) CaCl₂ solutions at the condenser side. See **Supplementary Note 2** for details on the reported error bars of experiments. Details on the parameters used in the theoretical models are reported in **Supplementary Tab. S1**.

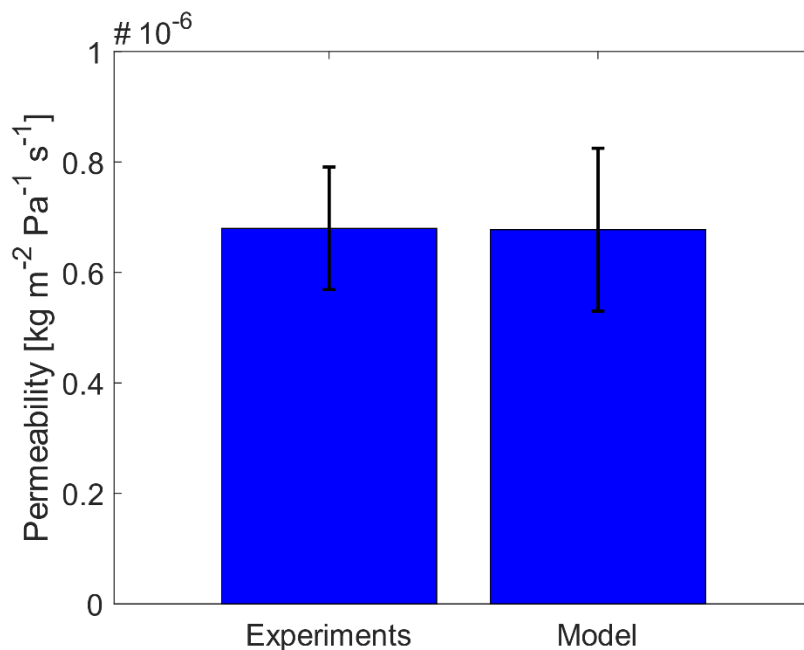


Fig. S5. Experimental results and modeling predictions of membrane permeability. The permeability of hydrophobic membrane is experimentally assessed according to the protocol described in the **Supplementary Note 1**. The membrane separates two cavities filled with distilled water and NaCl-water solution at 170 g L^{-1} , respectively. See **Supplementary Note 2** for details on the reported error bar of experiments. The model prediction is obtained by equation (13). The upper and lower bounds of the parameters employed for the modelling computations are shown in **Supplementary Tab. S1**: the modelled value of the membrane permeability is obtained by the average of the values from the different combinations of the three parameters listed, while the related error bar estimated considering their standard deviation.

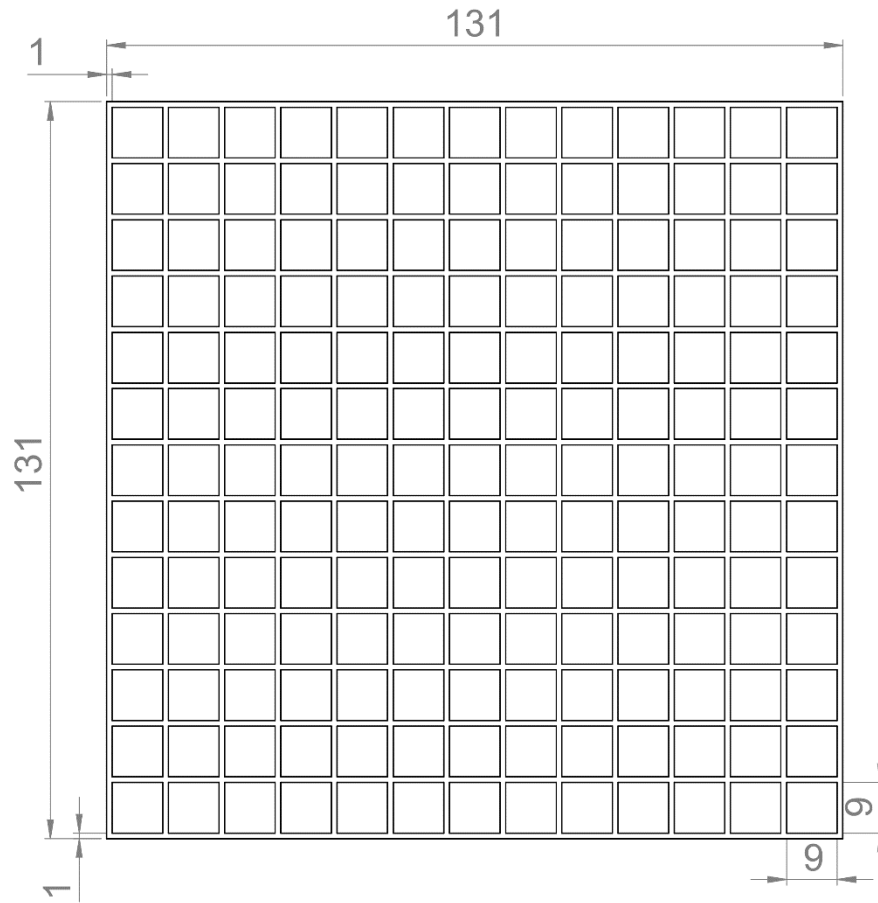


Fig. S6. Possible spacer for enhancing the cooler performance. Top view of a possible spacer that could be positioned between the hydrophilic layer acting as evaporator and the hydrophobic membrane to improve the cooling performance of the device. The resulting air gap has tortuosity $\tau = 1$ and porosity $\epsilon_a = 0.8$. The reported units are expressed as millimetres.

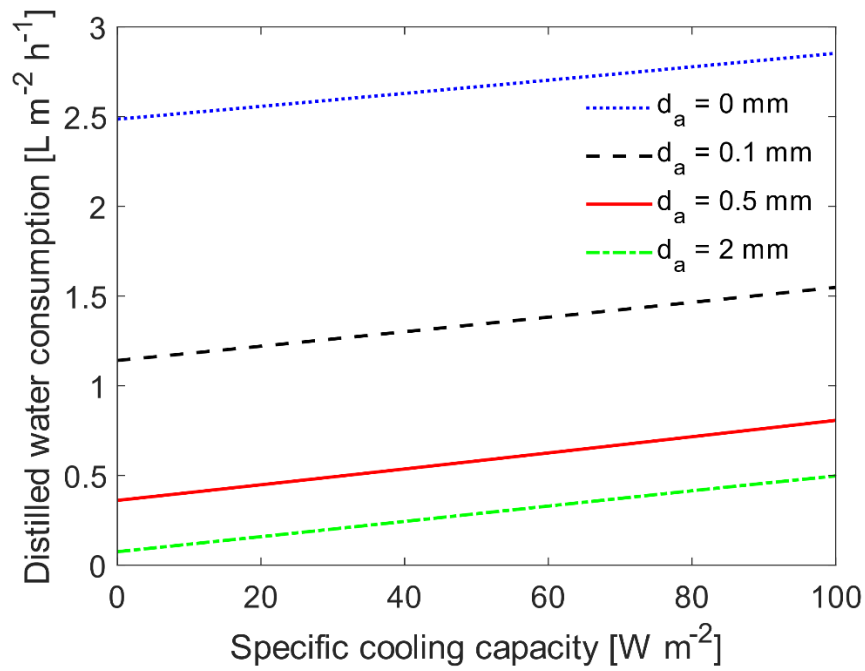


Fig. S7. Distillate consumption by the passive cooler for different air gaps. Modelling estimates for the distilled water consumption in the 4-stage passive cooler as predicted by the lumped parameter model, considering an additional air gap in series to the membrane. In detail, the performance of the cooling device are estimated varying the thickness of the additional air gap (d_a) from 0 to 2 mm, while considering a 3.1 molal NaCl solution in the condensers and $T_A = 30$ °C. All the model parameters employed are reported in the **Supplementary Tab. S1**.

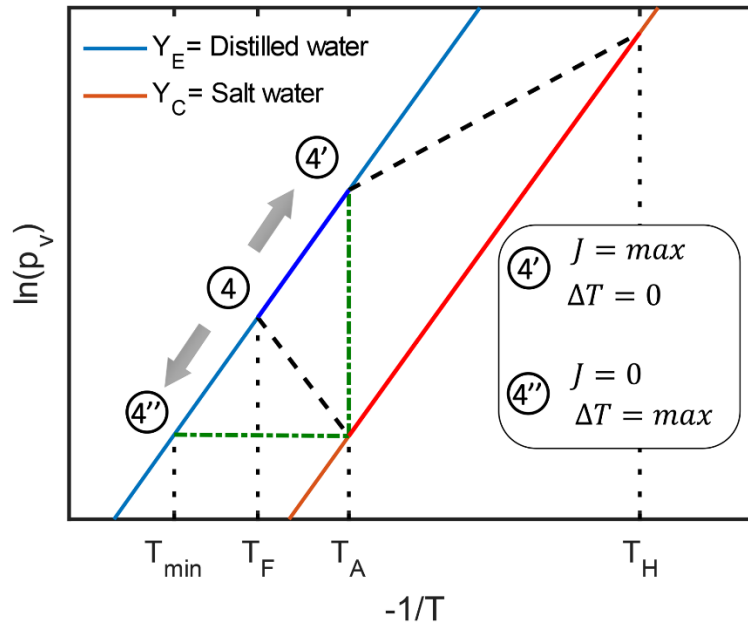


Fig. S8. Qualitative thermodynamic cycle of a passive solar cooling cycle. The qualitative thermodynamic cycle is drawn referring to single-stage cooling and distillation devices, and assuming the temperature of evaporators and condensers equal to those of the surrounding environments (T_F and T_A , respectively). The schematic of the coupling between the proposed cooling device and a passive solar distiller is reported in **Fig. 5**. Point (4) identifies a generic working temperature of the cooler (T_F), which is below the ambient temperature (T_A). Moving this operating point along the isosteric curve of distilled water (Y_E), points (4') and (4'') identify the extreme working conditions of the proposed device. On the one hand, (4') identifies the highest temperature of heat extraction ($T_F = T_A$), where the temperature difference across the device is null and the pressure difference across the membrane, thus the water vapour flux and the extracted heat, is maximum. This is evident also from equation (19), where the second term on the right-hand side should be zero under the ideal assumption that the condenser and evaporator temperatures equal the cold chamber and environment temperatures, respectively. On

the other hand, point (4'') identifies the lowest temperature of cooler operations ($T_F = T_{min}$), where the temperature difference across the device is maximum while the net water vapour flux is null.

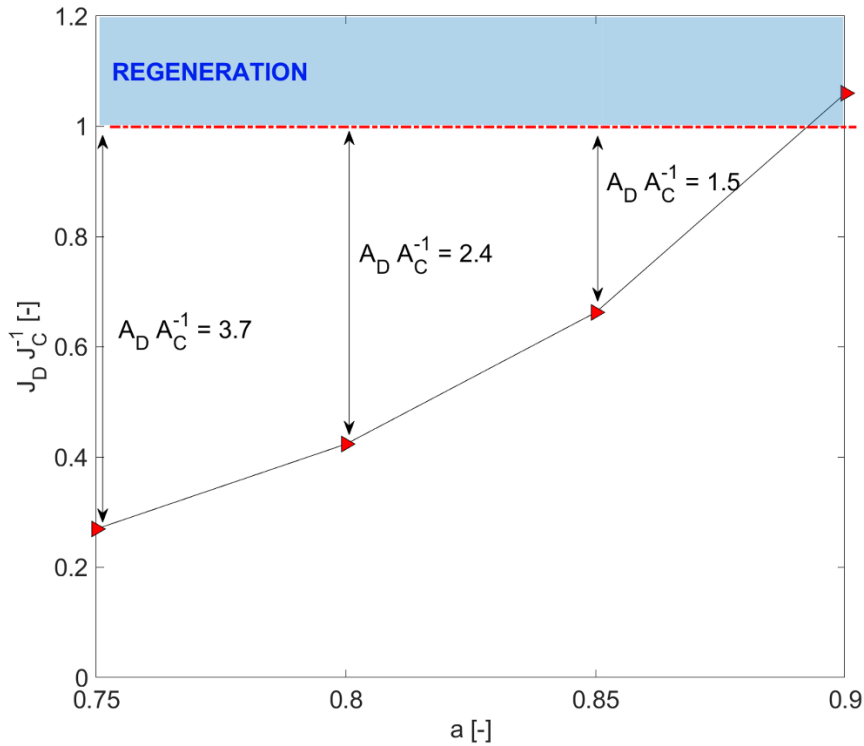


Fig. S9. Coupling between the passive cooler and distiller to implement a stable cooling

cycle. J_D and J_C are the distillate flow rates of distiller and the distillate water consumption of

cooler, respectively. a represents the activity of the processed salt water. $A_D = A_{Distiller}$ and

$A_C = A_{Cooler}$ are the areas of the distiller and cooler, respectively. To achieve efficient

regeneration of the progressively diluted salt solution, the ratio between the areas ($A_D A_C^{-1}$)

should be larger than 1. The reported estimates are referred to the following coupling parameters:

$R_S = 1$, $R_A = 1$ and N° of stages equal to 4. The specific cooling power is 100 W m^{-2} . See the

Supplementary Note 6 for details.

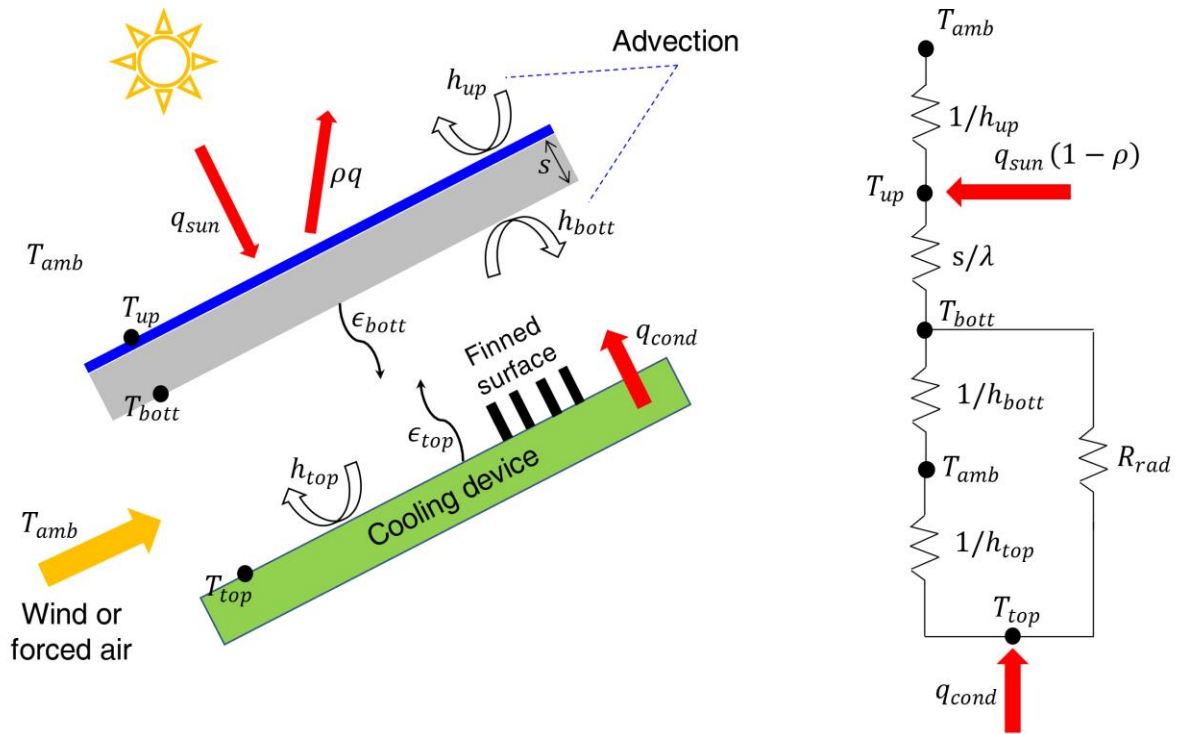


Fig. S10. Mirror screening of the cooler exposed to the sun. Left-hand-side: a solar shield can be used to prevent an excessive temperature lift at the top surface of the cooling device (*i.e.* last-stage condenser). Right-hand-side: one-dimensional thermal model of the shielded cooling device represented on the right-hand side. See the **Supplementary Note 11** for details.

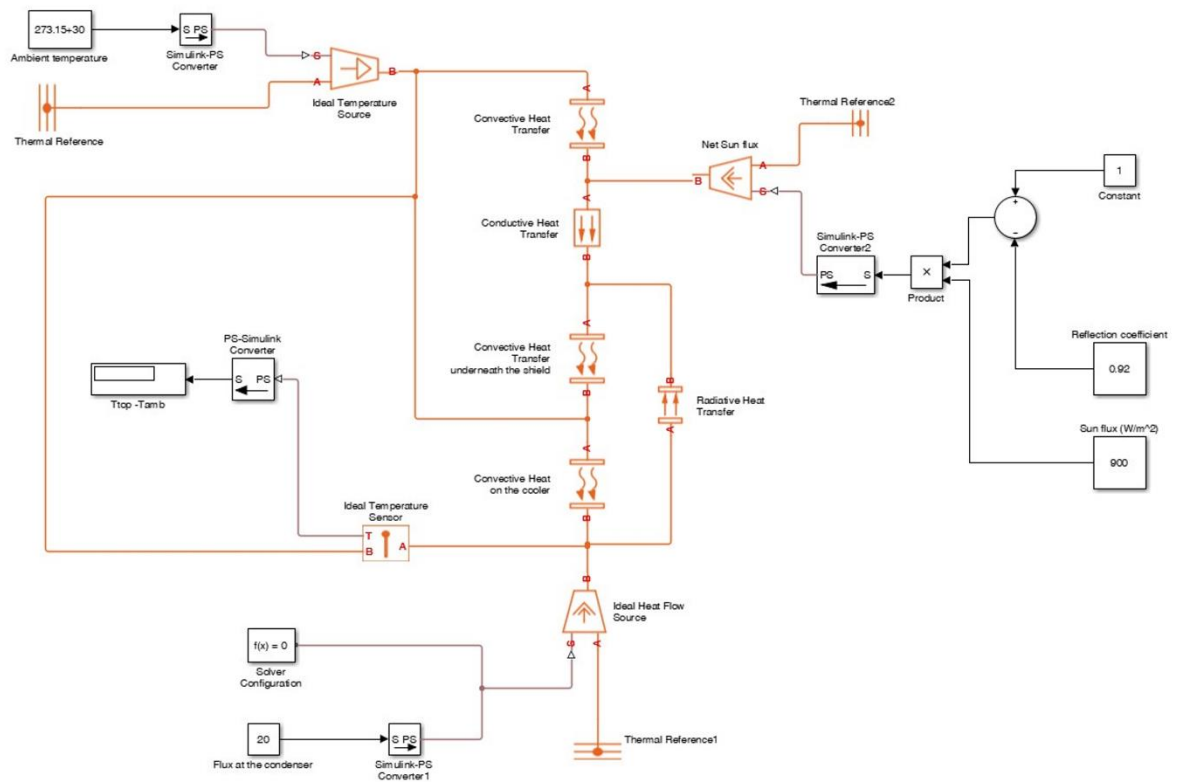


Fig. S11. SIMSCAPE implementation of the mirror screening of the cooler exposed to the sun. The reported blocks are equivalent to the lumped parameters model represented in the **Supplementary Fig. S10**. See the **Supplementary Note 11** for details.

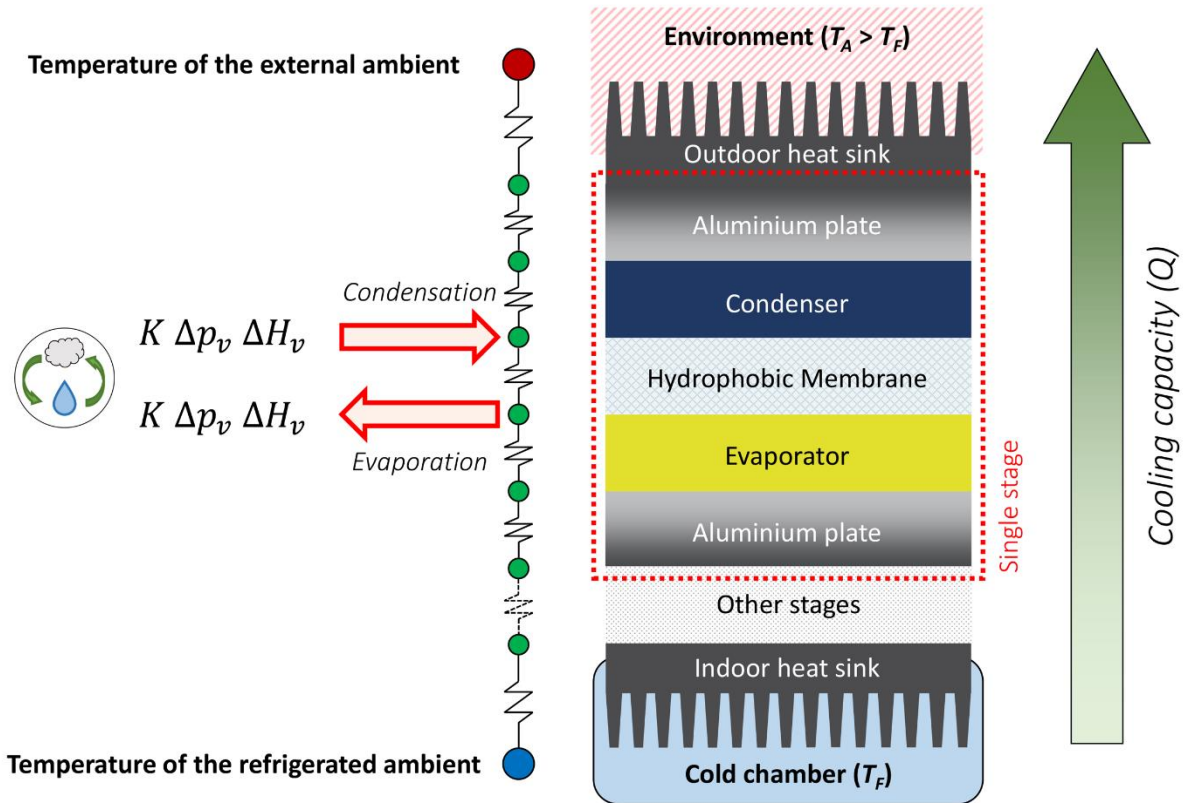


Fig. S12. Lumped model for the heat transfer in the passive cooler. The passive cooler allows to refrigerate a cold chamber, since it extracts heat from the cold chamber and discharge it to the environment. The lumped thermal resistances represented in the picture are associated with the components forming the stratigraphy of the multistage passive cooler. In particular, from top to bottom: convective resistance due to the heat sink placed between the top side of the cooling device and the environment; conductive resistance of the last-stage aluminium plate; conductive resistance of the last-stage condenser (salt water); conductive resistance of the last-stage membrane; conductive resistance of the last-stage evaporator (hydrophilic layer and distilled water); further conductive resistances provided by the additional N stages of the cooler; convective resistance due to the heat sink placed between the bottom side of the cooling device and the cold chamber (not present in the lab-scale tested prototype, as reported in

Supplementary Fig. S1). The evaporation and condensation of water in the evaporators and condensers generate the additional transfer of enthalpy of evaporation through the N stages (see the red arrows), which is responsible of the cooling capacity of the device.

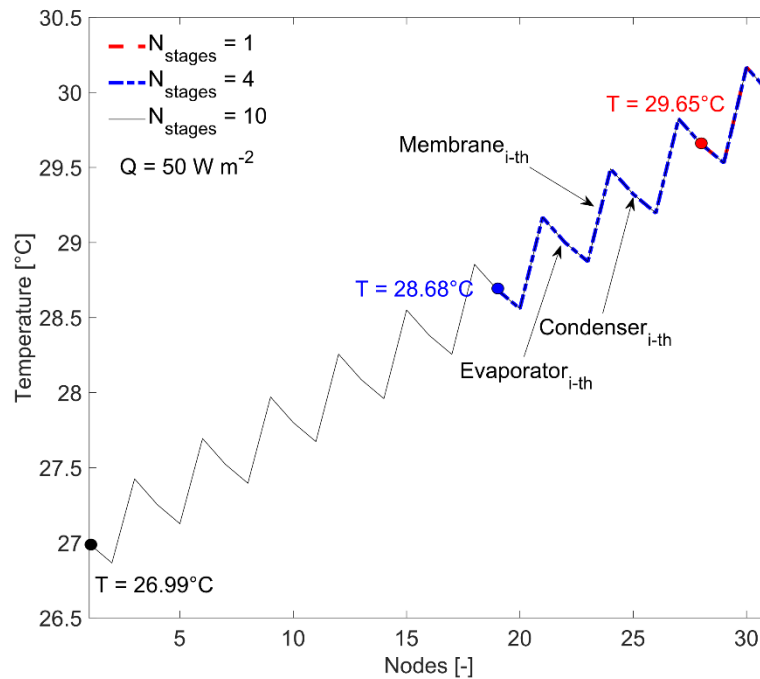


Fig. S13. Temperature profiles across the cooling stages in case of a 1-, 4-, and 10-stage configuration device. Results are obtained by the one-dimensional theoretical model considering a fixed specific cooling capacity 50 W m^{-2} and ambient temperature equal to $30 \text{ }^\circ\text{C}$. Each thermal resistance is defined between two consecutive nodes. For example, a single stage device is made of 4 nodes, namely condenser, condenser/membrane interface, membrane/evaporator interface and evaporator. Red, blue and black circles represent the temperature of the evaporator in contact with the colder room in case of a 1-, 4- and 10-stages

configuration device, respectively. Results show that, at fixed cooling capacity, the temperature difference ΔT is proportional to the number of stages.

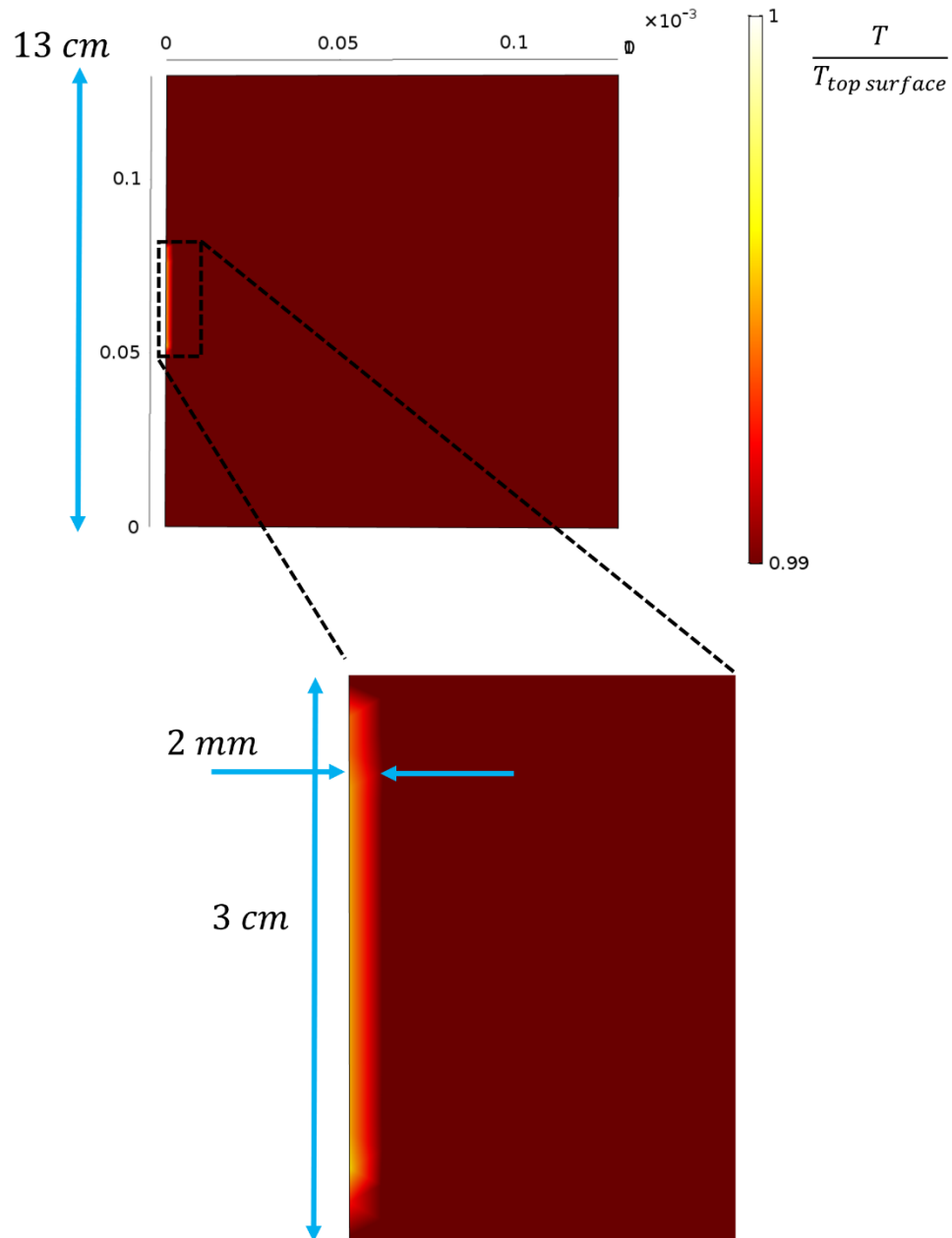


Fig. S14. Results of the finite element model for the hydrophilic layer (evaporator). The temperature distribution obtained by the finite element computation across the hydrophilic layer

is depicted. The temperatures are normalized with respect to the ambient one, to highlight the effect of boundaries on the temperature field. See the **Supplementary Note 13** for details.

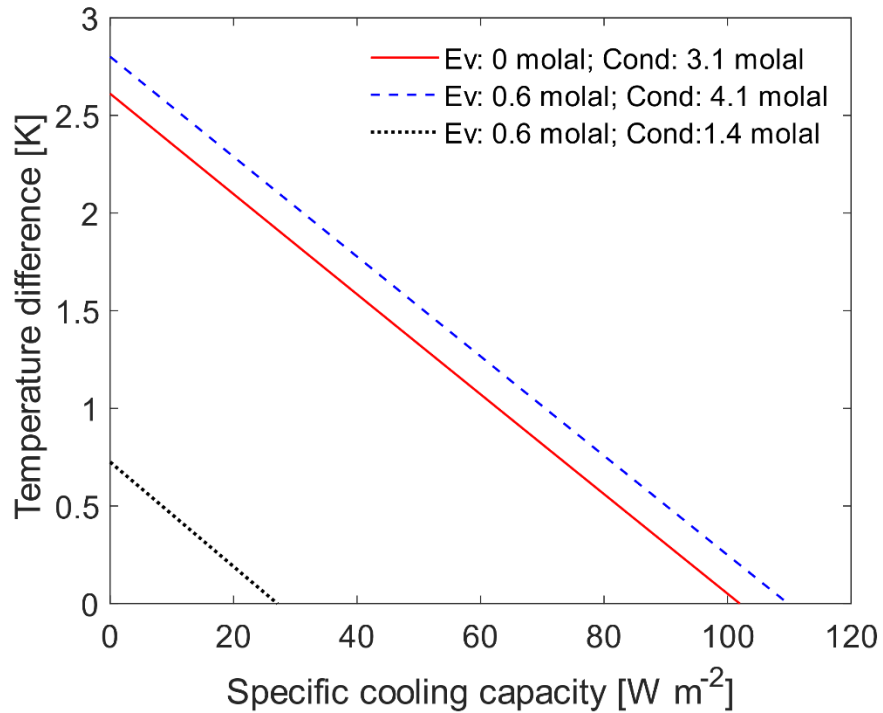


Fig. S15. Passive cooler operating with high-salinity brines produced by different desalination technologies. Characteristic curve of the passive cooler with different salt concentration in the solutions that feed its evaporators and condensers. Dashed blue line: seawater in the evaporators (35 g L^{-1} , 0.6 molal); brine in the condensers (220 g L^{-1} , 4.1 molal). Solid red line: distilled water in the evaporators (0 g L^{-1} , 0 molal); salt water in the condensers (170 g L^{-1} , 3.1 molal). Dotted black line: seawater in the evaporators (35 g L^{-1} , 0.6 molal); typical reverse osmosis brine in the condensers (80 g L^{-1} , 1.4 molal). See **Supplementary Note 8** for additional discussions and details.

Supplementary Tables

Table S1. Uncertainties in the theoretical model. Upper and lower values of variables in the lumped parameter model that have been adopted to determine the uncertainty of model estimations. In particular, the evaluation of the uncertainty on the activity coefficients of water in the different salt solutions are reported in **Supplementary Note 2**; the membrane porosity interval is taken similarly with common evidence in the literature (74, 75); the boundary values assigned to the membrane thickness are taken coherently with the data reported by the vendor. The temperature employed for the computations of the membrane permeability, reported in **Supplementary Fig. S5**, is approximately the average of the values experimentally assessed during the tests. The model predictions reported in **Fig. 3D** and **Supplementary Fig. S7** are done considering an air gap positioned between the hydrophilic layer acting as evaporator and the hydrophobic membrane. Those estimates consider a variable thickness (d_a), but fixed tortuosity ($\tau = 1$) and porosity ($\epsilon_a = 0.8$). The air gap adjacent to the membrane can be realized by polymeric (hydrophobic) grids/spacers. Considering the prototype of the passive cooler tested here (*i.e.* active area equal to $1.69 \times 10^{-2} \text{ m}^2$), such an air gap could be for instance implemented by means of the spacer represented in the **Supplementary Fig. S6**.

Plot	a [-]		ϵ_m [-]		d_m [μm]		T_A [$^{\circ}\text{C}$]
	Lower bound	Upper bound	Lower bound	Upper bound	Lower bound	Upper bound	
NaCl solution (Fig. 2, Fig. 3A, Sup. Fig. S4A)	0.8979	0.9009	0.75	0.85	105	115	30
CaCl ₂ solution (Fig. 3A, Sup. Fig. S4B)	0.8473	0.8659	0.75	0.85	105	115	30
Seawater (Fig. 3A)	0.9771	0.9800	0.75	0.85	105	115	30
Permeability (Sup. Fig. S5)	0.8979	0.9009	0.75	0.85	105	115	21
NaCl: Temperature sensitivity (Fig. 3B)	0.8998		0.8		110		-
NaCl: N. stages and air gap sensitivity (Fig. 3C, Fig. 3D, Sup. Fig. S7)	0.8998		0.8		110		30

Table S2. Exergy performance of the passive cooler with different number of stages. See the Supplementary Note 4 for details on these calculations.

N° stages	Q_{in} [W m^{-2}]	T_{in} [K]	G_{in} [kg s^{-1}]	η_{Carnot} [-]	Ψ_{in} [W m^{-2}]	$G_{in}b_{in}$ [W m^{-2}]	η_{II} [%]
1	50	302.80	1.89×10^{-4}	-0.0011	-0.05	-2.90	1.98
4	50	301.83	7.41×10^{-4}	-0.0043	-0.21	-11.38	1.92
10	50	300.14	17.81×10^{-4}	-0.0100	-0.50	-27.36	1.83

Table S3. Estimated costs for the prototype of passive cooler. See the Supplementary Note 9 for details on these calculations.

Material	Supplier	Unitary cost	Quantity	Total price [€]
PTFE membranes	ANOW microfiltration	26.8 [€/m ²]	$1.7 \cdot 10^{-2}$ [m ²]	0.45
Aluminium sheets	Wholesale	2.2 [€/kg]	$5.5 \cdot 10^{-2}$ [kg]	0.12
ABS frame	Wholesale	10.1 [€/kg]	$4.9 \cdot 10^{-2}$ [kg]	0.50
Hydrophilic layer	Henkel	9.0 [€/m ²]	$6.5 \cdot 10^{-2}$ [m ²]	0.58
Silicone pipes	Wholesale	0.4 [€/m]	0.6 [m]	0.27

Table S4. Estimated costs for the prototype of passive distiller considered here to implement a solar cooling cycle. See the Supplementary Note 9 for details on these calculations.

Material	Supplier	Unitary cost	Quantity	Total price [€]
PTFE membranes	ANOW microfiltration	26.8 [€/m ²]	$1.7 \cdot 10^{-2}$ [m ²]	0.45
Aluminium sheets	Wholesale	2.2 [€/kg]	$5.5 \cdot 10^{-2}$ [kg]	0.12
Hydrophilic layer	Henkel	9 [€/m ²]	$5.1 \cdot 10^{-2}$ [m ²]	0.46

Table S5. Parameters considered for the simulations of the cooler performance under the sun. See the **Supplementary Note 11** for details on these calculations.

Sun flux [Wm ⁻²]	Solar reflectance [-]	Cooler flux [Wm ⁻²]	Advection coefficient [Wm ⁻² K ⁻¹]	Insulator thickness [m]	Insulator thermal conductivity [Wm ⁻¹ K ⁻¹]	Advection coefficient [Wm ⁻² K ⁻¹]	Optical emissivity [-]	Temperature difference [K]
q_{sun}	ρ	q_{cond}	h_{up}	s	λ	$h_{bott} \approx h_{top}$	$\epsilon_{bott} \approx \epsilon_{top}$	$T_{top} - T_{amb}$
1000	0.92	20	3	5e-2	0.04	100	0.1	0.095
1000	0.85	20	3	5e-2	0.04	100	0.1	0.12
1000	0.92	20	3	5e-2	0.04	50	0.1	0.24
1000	0.92	100	3	5e-2	0.04	50	0.1	0.76
1000	0.92	100	3	5e-2	0.04	100	0.1	0.39
500	0.92	100	3	5e-2	0.04	100	0.1	0.37
1000	0.92	100	3	5e-2	0.04	150	0.1	0.27